Supplementary Information

Microparticles with hetero-nanointerfaces: controlled assembly of cobalt hydroxide and nickel hydroxide nanoclusters towards improved electrochemical functions.

Naoki Tarutani[a], Yasuaki Tokudome[a], Matías Jobbágy[b], Galo J. A. A. Soler-Illia[c]*, Masahide Takahashi[a].*

[a]*Department of Materials Science, Graduate School of Engineering, Osaka Prefecture University, Sakai, Osaka 599-8531, Japan*
[b]*INQUIMAE-CONICET, Facultad Ciencias Exactas y Naturales, Universidad de Buenos Aires, Buenos Aires, C1428EHA, Argentina*
[c]*Instituto de Nanosistemas, Universidad Nacional de General San Martín, Av. 25 de Mayo y Francia, San Martín, 1650, Argentina.*

Characterization.

SAXS measurement.

The small angle X-ray scattering (SAXS) measurement was performed to characterize formed particle size and mesostructures with the beamline of the Brazilian Synchrotron Light Laboratory (LNLS, Brazil D11A-SAXS1-18927 and 20160366). X-ray with a wavelength, λ, of 0.1544 nm was used. A linear position sensitive X-ray detector and a multichannel analyzer were used to collect the SAXS signal. For in-situ analysis, SAXS patterns were collected every 1 min (45 s for accumulation time and 15 s for dead time). The first pattern was collected reaction time from 1.5 to 2.5 min, which is denoted as pattern of 2 min reacted solution. A sample-to-detector distance was set at 904.6242 mm, corresponding scattering vector range of 0.1−4.8 nm^{-1}. After the removal of background, the scattering profiles were circular averaged and plotted against the scattering vector, q, according to the following equation;

$$q = \frac{\pi}{\lambda}\sin 2\theta$$

where θ is scattering angle. To evaluate particle size from experimental SAXS patterns, we employed a unified equation proposed by Beaucage and Schaefer [Beaucage, G.; Schaefer, D.W. *J. Non-Cryst. Solids* **1994**, *172-174*, 797-805.; Beaucage, G. *J. Appl. Cryst.* **1995**, *28*, 717-728.], which was developed to describe scattering from objects with hierarchical structures. The unified equation for the hierarchical structure with multiple structural levels is described as follows;

$$I(q) \approx \sum_{i=1}^{n}\left(G_i \exp\left(\frac{-q^2 R_{gi}^2}{3}\right) + B_i \exp\left(\frac{-q^2 R_{g(i+1)}^2}{3}\right) \times \left\{\left[erf\left(\frac{qR_{gi}}{\sqrt{6}}\right)\right]\right\}^{P_i}\right)$$

where n is the number of structure levels, R_{gi} is the gyration radius of the ith level, P_i is the power-law exponent, G_i is the Guinier prefactor, and B_i is the prefactor specific to the type of power-law scattering falls. The particle diameter of ith level, D_i, is calculated by using spherical particle model as follows;

$$R_{gi} = \frac{D_i}{2}\sqrt{\frac{3}{5}}$$

Considering the sample-to-detector distance, the structures over ~ 30 nm is difficult to calculate by fitting of SAXS patterns.

XPS measurement.

The sample powders were mounted on polished indium plate and pressed without adhesives. Survey spectra and high-resolution spectra were collected with a step of 0.4 and 0.125 eV, respectively. 0.05 eV for C 1s, O 1s, Ni $2p_{3/2}$, Co $2p_{1/2}$. For each XPS analysis, the sample was exposed to the X-rays for less than 2 h. Spectra were analyzed using MultiPak software. Input parameters for the curve resolution procedure included the number of peaks and the peak intensity, peak width at half

maximum, and position for each individual peak. The instrument work function was calibrated to give an Au $4f_{7/2}$ of metallic gold binding energy of 83.95 eV±0.1 eV. Spectra from samples were shifted to give the C 1s spectral component a binding energy of 284.8 eV.

Electrochemical measurement.

To stabilize the sample materials, cyclic voltammetry measurement was applied before all of electrochemical measurements as a pre-activation (scan speed was 100 mV/s; potential window of 0 to 0.50 V; test cycle was at least 20 runs). The cyclic voltammetry measurements were performed at various scan rates of 5, 10, 25, 50 and 100 mV/s within a potential window of 0 to 0.50 V. The double layer capacitances (C_{dl}) were determined to estimate electrochemically active surface area. The potential window of cyclic voltammetry curves was 25–75 mV with a scan rate of 20, 40, 60, 80, 100, and 120 mV/s. C_{dl} was estimated from linear fitting of a plot of current density Δj versus scan rate ($\Delta j = j_a - j_c$ at 50 mV). The charge/discharge measurements were performed within a potential window of 0.05 to 0.50 V at different current densities of 1, 2, 5, 10, 15 and 20 A/g. The electrochemical impedance spectroscopy measurements were performed at frequencies ranging from 10^5 to 10^{-1} Hz with an amplitude of 5 mV at a potential of corresponding oxidation peak position.

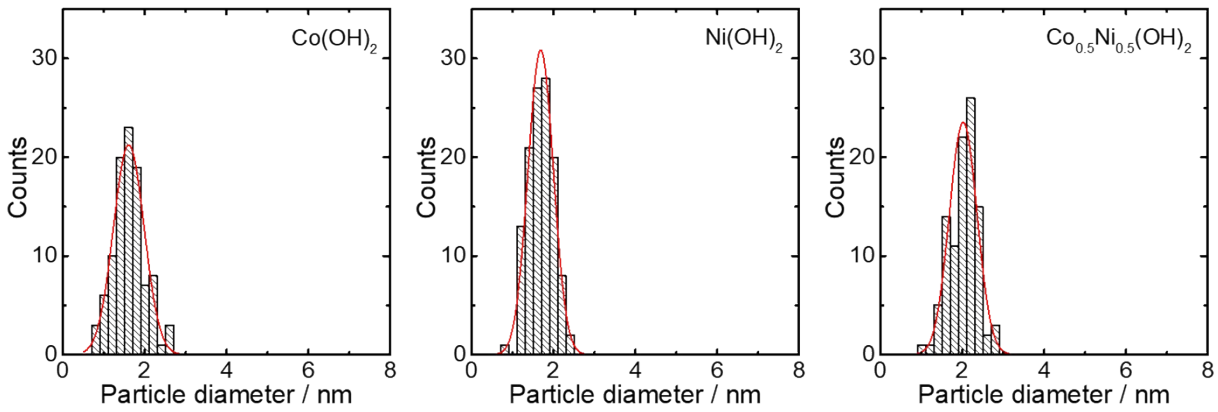

Fig. S1 Particle size distributions of $Co(OH)_2$, $Ni(OH)_2$, an $Co_{0.5}Ni_{0.5}(OH)_2$ nanoclusters. The particle diameters were estimated from TEM images.

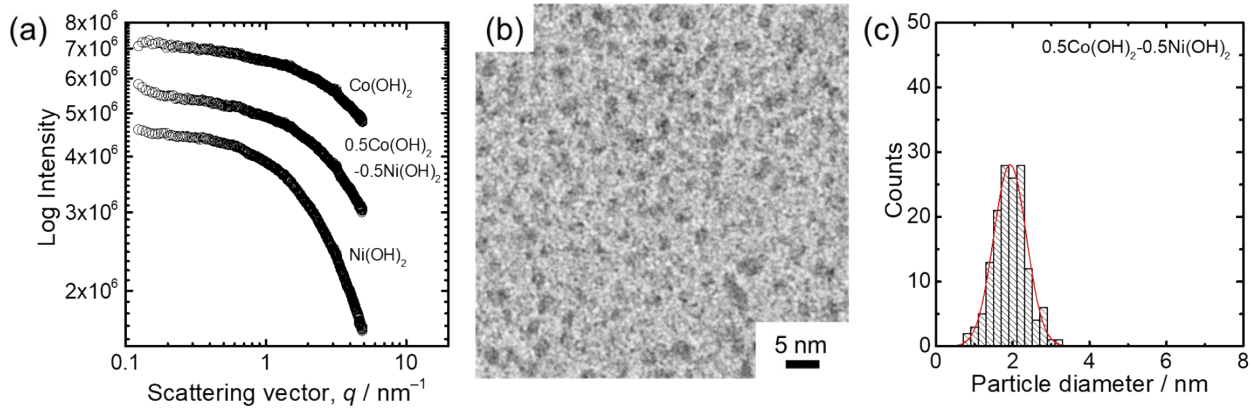

Fig. S2 (a) SAXS patterns of $Co(OH)_2$, $Ni(OH)_2$ and $0.5Co(OH)_2$-$0.5Ni(OH)_2$ nanocluster colloids (60 min after addition of PO). (b) TEM image and (c) corresponding particle size distribution of $0.5Co(OH)_2$-$0.5Ni(OH)_2$ nanocluster.

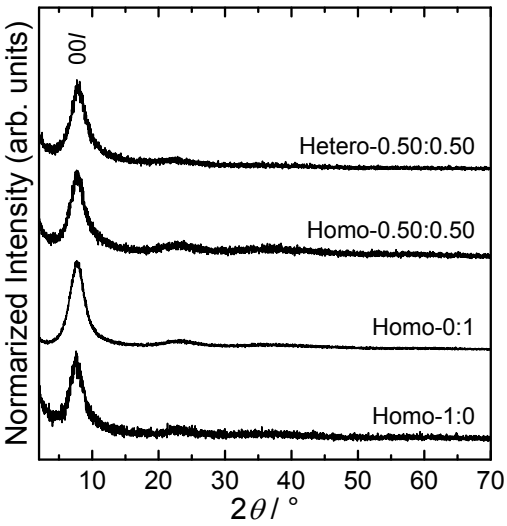

Fig. S3 PXRD patterns of Homo-1:0, Homo-0:1, Homo-0.50:0.50, and Hetero-0.50:0.50.

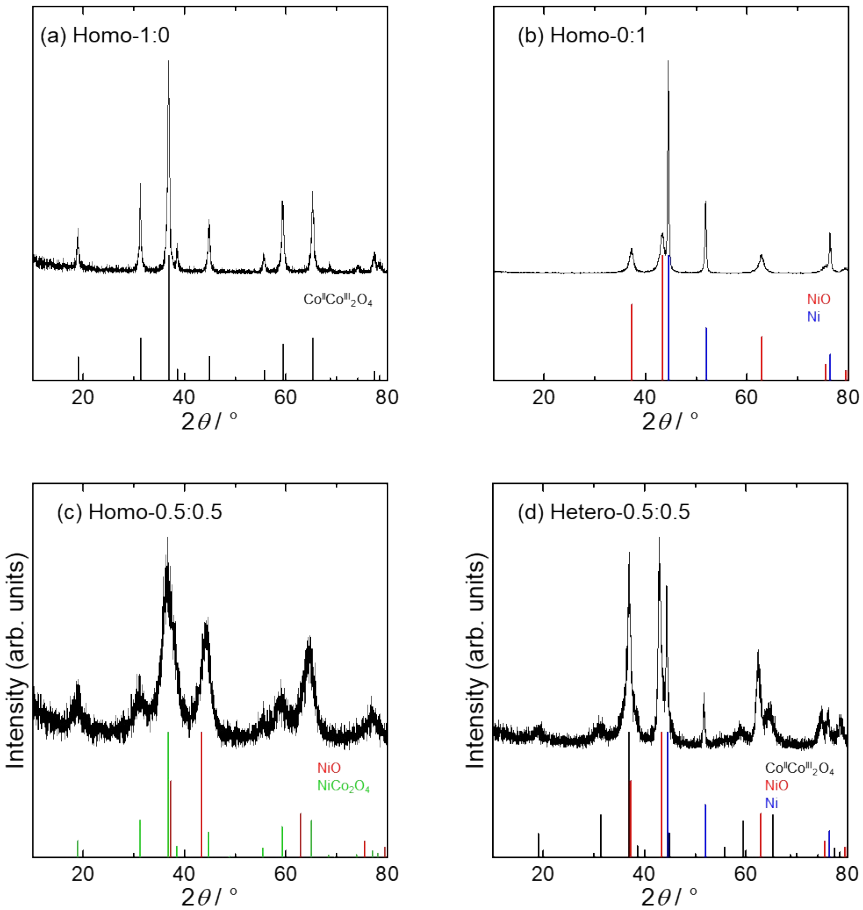

Fig. S4 XRD patterns of (a) Homo-1:0, (b) Homo-0:1, (c) Homo-0.5:0.5, and (d) Hetero-0.5:0.5 after heat-treatment at 300 ˚C for 2 h (ramp rate was 2.5 ˚C/min, under air flow of 2 L/min). The vertical bars show the peak positions of Co(II)Co(III)$_2$O$_4$ (black, 00-042-1467), NiO (red, 00-047-1049), Ni (blue, 00-004-0850), and NiCo$_2$O$_4$ (green, 00-073-1702).

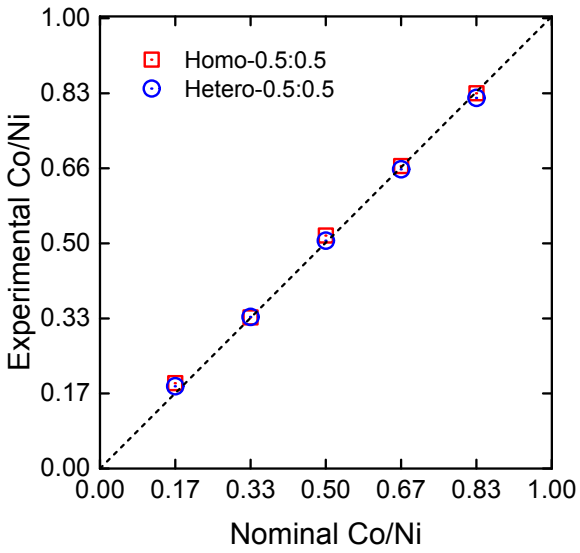

Fig. S5 Relationship of nominal molar ratio Co/Ni and experimental Co/Ni of Homo-x:1−x and Hetero-y:1−y ($0 \leq x \leq 1$, $0 < y < 1$). The experimental value was estimated from EDS spectra.

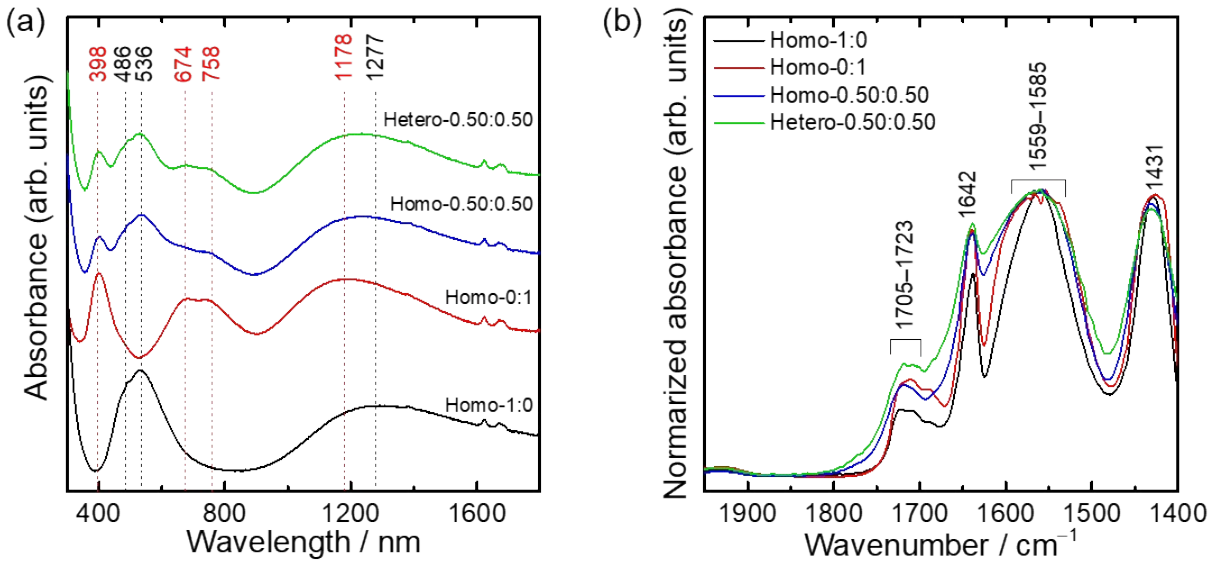

Fig. S6 (a) UV-Vis-NIR and (b) IR spectra of Homo-1:0 (black), Homo-0:1, (red), Homo-0.50:0.50, (blue) and Hetero-0.50:0.50 (green) microparticles. The peaks shown in (a) are assigned as follows; the peaks of 486, 536, and 1277 nm are transitions of $^4T_{1g}$(F) to $^4T_{1g}$(P), $^4A_{2g}$(F), and $^4T_{2g}$(F) of octahedral coordinated Co(II), respectively; the peaks of 398, 674, 758, and 1178 nm are transitions of $^3A_{2g}$ to $^3T_{1g}$(P), $^3T_{1g}$(F), ^1E_g(D), and $^3T_{2g}$(F) of octahedral coordinated Ni(II), respectively (The peaks around 1620−1680 nm are overtones of ν(OH) vibrations of acrylic acid). The peaks in (b) were as follows; 1431, 1559−1585, 1642, 1705−1723 cm^{-1} are $\nu(COO)_s$, $\nu(COO)_{as}$, ν(C=C) of acrylate, ν(C=C) of acrylic acid, and ν(OH) of acrylic acid respectively. The vibration difference of symmetric and asymmetric COO vibrations ($\Delta = \nu(COO)_{as} - \nu(COO)_s$) reveals chemical condition of carboxylic acids [Feairheller, W. R.; Katon, J. E., *Spectrochim. Acta* **1967**, *23*, 2225–2232.]. Δ of obtained materials were 128−154 cm^{-1}. Comparing with Δ of free acrylate (110−140 cm^{-1}) [Deacon, G.B.; Phillips R.J., *Coord. Chem. Rev.* **1980**, *33*, 227-250.], it is estimated that acrylates are unidentate coordinated, intercalated, and adsorbed onto hydroxide layers.

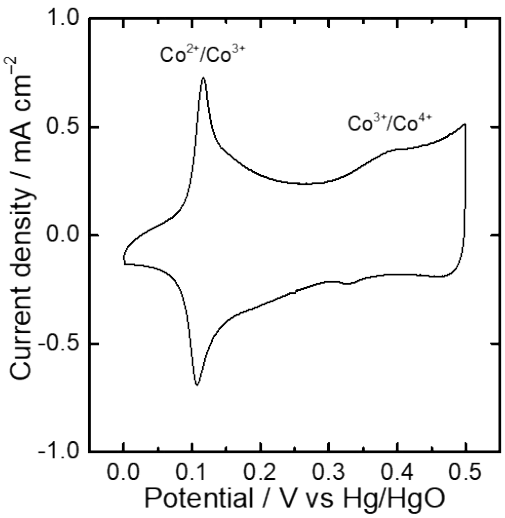

Fig. S7 CV curve of Homo-1:0 recorded at a scan rate of 100 mV/s.

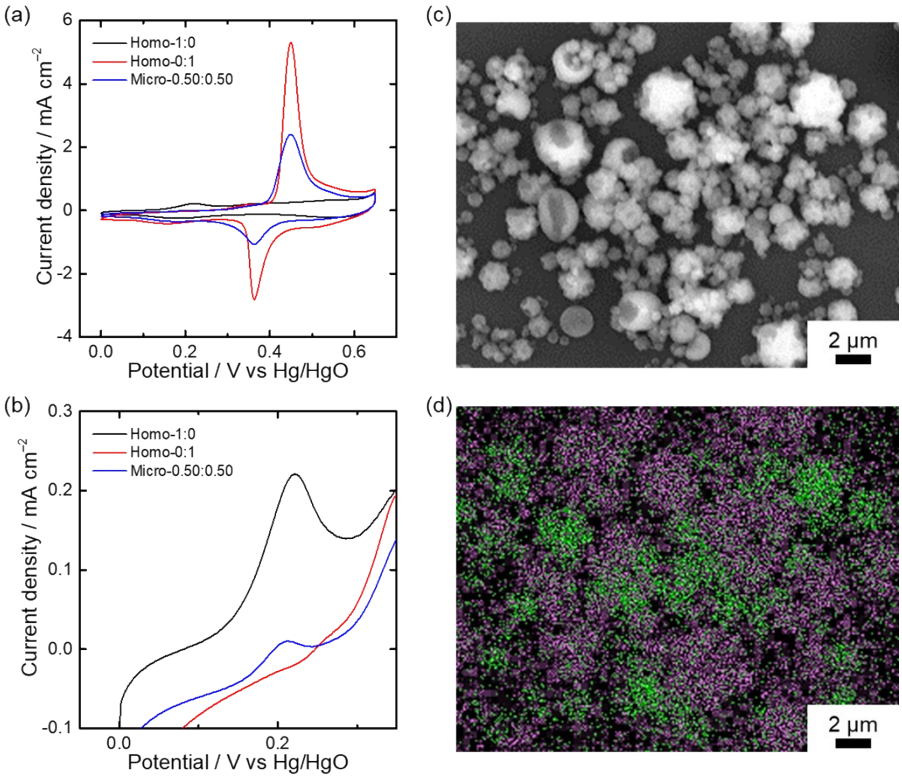

Fig. S8 CV curves of Homo-1:0, Homo-0:1, and Micro-0.50:0.50 recorded at a scan rate of 100 mV/s. The powders of Homo-1:0 and Homo-0:1 were dispersed in toluene (10 g/L). Micro-0.50:0.50 was prepared by mixing equal amount of suspensions of Homo-1:0 and Homo-0:1. 2 μL of obtained suspensions were deposited onto Au electrode and dried at room temperature. (c) SEM image and (d) EDS mapping image (green: Ni, purple: Co) of Micro-0.50:0.50 deposited onto Si substrate. Here, oxidation/reduction peaks of Micro-0.50:0.50 did not shift significantly (Fig. S7a and S7b), which indicates that formed hetero-microinterfaces (Fig. S7d) did not give an effective contribution on electrochemical reaction.

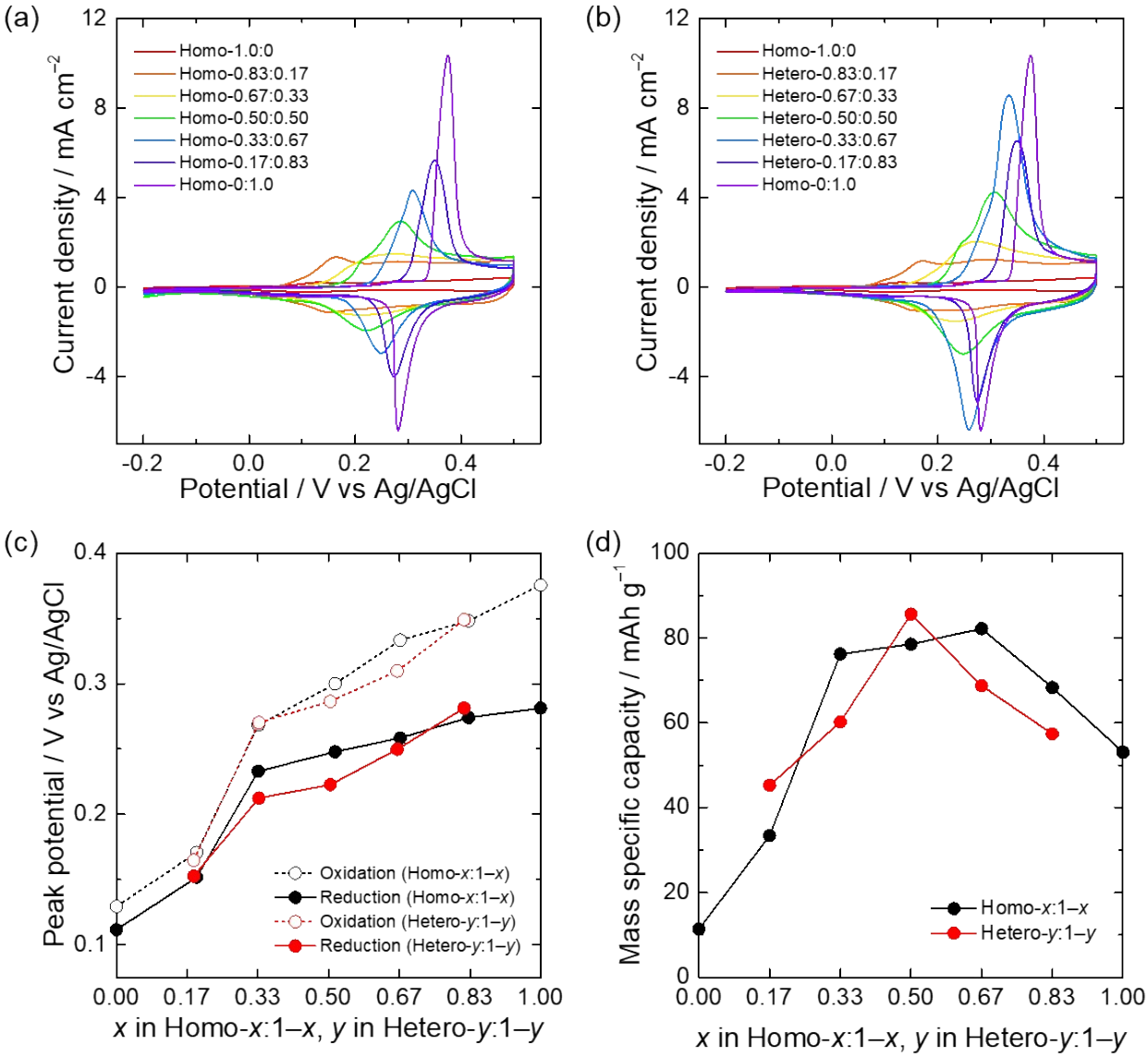

Fig. S9 CV curve of (a) Homo-x:1−x and (b) Hetero-y:1−y ($0 \leq x \leq 1$, $0 < y < 1$) at scan rate of 100 mV/s. (c) The oxidation/reduction peak potentials and (d) mass specific capacities of Homo-x:1−x and Hetero-y:1−y ($0 \leq x \leq 1$, $0 < y < 1$). The peak positions and mass specific capacities were estimated from respective CV curves recorded at a scan rate of 100 mV/s shown in (a) and (b).